The Effect of Inlet and Outlet Pattern on a Parabolic Dome Solar Collector

Phoothanet Saengcharoon and Orawan Aumporn*

Department of Physics, Faculty of Science, Silpakorn University, Nakhon Pathom, 73000, Thailand

* Corresponding author. E-mail address: Aumporn_O@su.ac.th

Received: 22 April 2026; Revised: 29 May 2026; Accepted: 15 June 2026; Available online: 1 June 2026

Abstract

This research aims to investigate the effects of air inlet and outlet patterns on parabolic-dome solar collectors. A three-dimensional transient computational fluid dynamics (CFD) simulation in ANSYS Fluent was used to analyze sixteen different inlet-outlet patterns and compare their effects on air behavior, outlet air temperature, and thermal efficiency. Simulation results show that most patterns led to recirculating air, resulting in hot spots and reduced heat transfer efficiency. Conversely, pattern 3-2 exhibited the most uniform air distribution. This 3-2 pattern also had an outlet air temperature and average thermal efficiency of about 42.75°C and 41.97%, respectively. Furthermore, the numerical model was validated using statistical indicators R^2, MRD, and RMSE, which showed that the model results were highly consistent with the experimental results (R^2 = 0.9942, MRD = -0.031°C, and RMSE = 3.656°C). These observations underscore the critical role of the inlet-outlet pattern in optimizing airflow and improving heat transfer efficiency. Therefore, this study presents an effective design for air inlet-outlet patterns that improves the efficiency of parabolic dome solar collectors through an optimized air channel design.

Keywords: inlet and outlet patterns, parabolic solar collector, solar energy

Introduction

Currently, global warming has intensified due to increased energy demand and consumption, resulting in erratic weather patterns. These phenomena have profound implications for socioeconomic impacts worldwide. To reduce reliance on fossil fuels, which are a major source of greenhouse gases, replacing them with clean and sustainable energy sources such as hydropower, wind power, and solar power is becoming increasingly popular (Stevovic et al., 2021; Østergaard et al., 2023; Singh and Kumar, 2025). Solar power, in particular, is more accessible than other energy sources in terms of cost, operation simplicity, and maintenance.

Solar energy is a clean energy source that can be used directly, such as in photosynthesis in plants and post-harvest processes, such as solar drying. Furthermore, it can be converted into electricity and hot water. However, despite its high potential and being environmentally friendly, its practical application still has some limitations, such as the inconsistency of sunlight from day to day or season, which makes energy production uncertain or less than desired. The utilization of solar energy through solar collectors is a highly attractive technology due to its potential to efficiently convert solar radiation into thermal energy (Omeiza et al., 2024; Lingayat et al., 2025).

Solar collectors function by absorbing solar radiation via a heat receiver, which may be a tube filled with a working fluid or an absorber plate. Subsequently, this receiver transfers heat to the working fluid (Duffie et al., 2020). The resulting heated fluid can then be employed in diverse industrial applications, including steam production, building heating, and drying processes (Aghakhani & Afrand, 2022; Famiglietti et al., 2020). Conversely, improving the thermal efficiency of solar collectors remains a major research area, to maximize solar energy use. However, the practical use of solar collectors is limited by several factors. In particular, the efficiency of heat transfer is reduced when sunlight is less intense, such as during cloudy weather or at night. Moreover, a substantial reduction in system efficiency stems from heat loss via conduction, convection, and radiation from the collector to the environment. It is therefore essential to design solar collectors to minimize such heat loss. This involves studying the effects of various components of a parabolic air heater, as in the work of Demissie et al. (2019), who designed, developed an indirect solar food dryer, and employed Computational Fluid Dynamics (CFD) to predict the transient three-dimensional flow field and temperature distribution within the drying chamber. The predicted airflow distribution showed that mean flow velocity varied across rack shelves, with a significantly more uniform distribution observed on the upper three shelves compared to the bottom shelf. The inside of the drying chamber evolved towards a steady operating temperature of 315 K, and the maximum average temperature difference between measurement and simulation was 4.3°C, confirming the reliability of CFD for solar dryer design. Hajiyat et al. (2023) similarly employed CFD simulation with COMSOL Multiphysics to investigate the effect of inlet size and location on greenhouse dryer process dynamics. The results showed that inlet size is positively correlated with average air velocity and negatively correlated with average temperature inside the dryer, while inlet location significantly impacts the spatial distribution of both temperature and velocity. It was concluded that dryer operating temperature and drying rate can be controlled through simple modifications of inlet size and location, highlighting the critical role of inlet geometry in solar dryer design. Rahmat et al. (2025) used CFD modeling to analyze the effects of various air inlet-outlet arrangements (specifically, upward, cross, and downward airflow configurations) on temperature distribution and air velocity. The simulation was performed using Ansys Fluent software, considering factors such as airflow rate and solar radiation intensity. The results demonstrated that the configuration with a downward airflow pattern (air inlet on the side and outlet at the bottom) yielded the most uniform temperature and air velocity distributions, resulting in the best drying efficiency. Furthermore, airflow itself affects air distribution, which is a crucial factor in heat exchange within the system. Kumar et al. (2021) developed a vacuum tube solar collector equipped with an internal air diverter under simulated solar light. It was found that thermal efficiency directly correlated with the air flow rate (100 – 1000 kg/h). Heat transfer increased with an increase in the airflow rate and the length of the air diverter. However, elevated inlet air temperatures (30 – 70°C) resulted in decreased heating efficiency. Similar to previous work by Kherrafi et al. (2025), conducted an experimental and numerical study to enhance the performance of a direct solar dryer integrated with obstacles. Using ANSYS Fluent simulations validated against experimental data, they investigated how internal obstacle configurations affect airflow distribution and thermal efficiency. The results demonstrated that optimized obstacle placement significantly improved airflow uniformity and heat transfer, reducing stagnant zones within the drying chamber and enhancing overall drying performance.

Previous research has demonstrated that air inlet, outlet, and airflow design directly affect the thermal efficiency of solar systems. While airflow optimization using CFD is common for rectangular or greenhouse solar dryers, a parabolic dome solar collector (PDSC) behaves differently due to its unique geometry. The curved dome often causes localized flow stagnation and uneven thermal stratification that standard designs cannot adequately address. Additionally, the parabolic shape captures sunlight throughout the day and reduces solar radiation reflection off the cover, enhancing the greenhouse effect inside the solar collector. To address this research gap, this study investigates how various inlet and outlet configurations affect fluid flow and heating efficiency under a no-load scenario, aiming to find the optimal flow mechanism to maximize heat transfer.

Materials and Methods

Solar collector model

ANSYS Workbench was employed to simulate airflow and heat energy transfer between components. The collector has a parabolic shape, 1 m wide, 0.6 m long, and 0.4 m high (Figure 1a). These dimensions were derived by scaling down from a full-sized parabolic greenhouse solar dryer (Janjai et al., 2009). The solar dryer is 5.5 m wide, 8.0 m long, and 3.5 m high. The length of the original drying chamber was reduced to minimize material consumption and computational resources while preserving the geometric proportions necessary for representative airflow simulation. The cover is made of a polycarbonate sheet. A black-painted galvanized steel sheet was used on the solar collector base. The air inlet and outlet dimensions were 40 × 5 cm^2 for the long air channel and 20 × 5 cm^2 for the short air channel (Figure 1b). The thermal properties of the solar collector components are shown in Table 1.

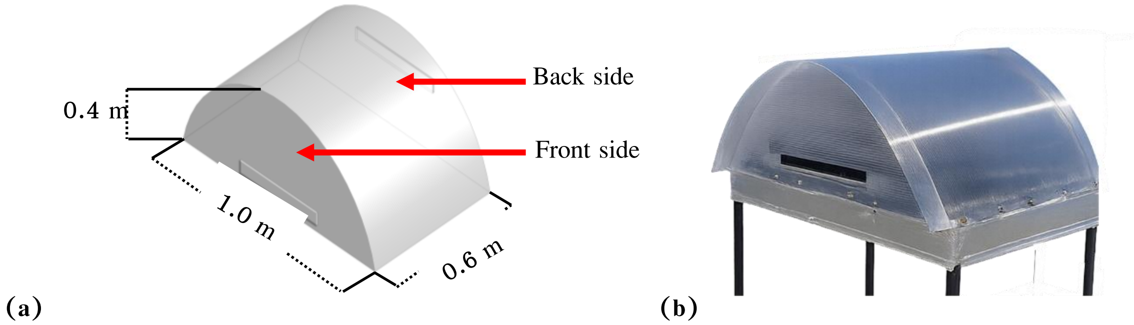

Figure 1 (a) Structural dimensions of the parabolic dome solar collector, and (b) Actual parabolic dome solar collector

Table 1 Thermal properties of the solar collector components

Name	Density (kg/m^3)	Specific heat (J/kg·K)	Thermal conductivity (W/m·K)
polycarbonate	1159.8	1192	0.20035
galvanized sheet	7849.8	481.98	51.962

Simulation Setup

For the analysis of heat transfer and fluid flow behavior in this research, ANSYS Workbench software was used. A 3D model of the PDSC was created using ANSYS DesignModeler, as shown in Figure 1a. The mesh size was 2 cm, the number of elements was 192955. Subsequently, a high-quality mesh was generated for each domain to ensure reliable and accurate simulation results. The mesh quality fell within the acceptable range based on multiple indicators (element quality = 0.849, aspect ratio = 1.803, skewness = 0.207, and orthogonal quality = 0.791). The fluid flow within the collector was modeled as turbulent using the standard k-ε turbulence model. This model was selected due to its well-established numerical robustness, computational economy, and proven capability in predicting macroscopic thermal performance and airflow distribution trends within solar thermal systems under no-load scenarios, particularly in fully turbulent flows with high Reynolds numbers. The numerical solution was governed by a pressure-based solver framework, utilizing the SIMPLE algorithm for pressure-velocity coupling. No-slip boundary conditions were enforced on all solid surfaces. To achieve high-order accuracy in spatial discretization, second-order upwind schemes were applied to solve the conservation equations of mass, momentum, and energy. Regarding solution convergence, the absolute residual criteria were strictly monitored and set to below 10^{-3} for the continuity, momentum (x, y, and z velocities), and turbulence quantities (k and ε). Crucially, to ensure a highly rigorous thermal evaluation, the convergence criterion for the energy equation was set to a more stringent threshold of below 10^{-6}. Simulations progressed continuously until all monitored residuals flattened and satisfied these prescribed limits before data extraction.

Boundary Conditions

In this simulation, boundary conditions were established to closely replicate real-world operating conditions. The cover sheet was set to be transparent with 80% transmission and 10% absorption. The galvanized steel sheet, painted black, was set as an opaque material with 80% absorption. Solar radiation intensity varied over time using the solar load model function of Fluent. Boundaries were set as walls to connect the fluid and solid boundaries. The following assumptions were used in the simulation:

- The inlet air temperature was set to a constant value according to the initial ambient temperature.
- There is no heat loss to the environment through the walls of the solar collector.
- The thermal properties of air and the different parts of the solar collector are constant because the temperature difference is very small.
- The cover sheet is set as a semi-transparent material with solar radiation transmission of 0.8 and solar radiation absorption of 0.1.

Governing Equations

As described above, ANSYS Workbench software was used in this research. The software contains a module for analyzing heat transfer and the behavior of air flow inside the PDSC. This was simulated using conservation equations for mass, momentum, and energy. The simulation was conducted in an unsteady (transient) and turbulent manner using the Fluent module in ANSYS software (Tuncer et al., 2023; Kherrafi et al., 2025).

- Continuity Equation

The continuity equation represents the principle of conservation of mass within the simulation domain. It states that the rate of change of fluid density over time at any position must be balanced by the net mass flux flowing into and out of the control volume, as expressed in Equation (1):

$$\frac{\partial \rho}{\partial t} + \nabla \cdot (\rho \vec{v}) = 0 \qquad (1)$$

Where ρ is air density (kg/m³)

t is time (s)

$\vec{v}$ is velocity vector (m/s)Momentum Equation

The momentum equation is based on the principle of conservation of momentum (Newton's second law of motion), describing the dynamic behavior of the fluid under various forces. The equation is given as follows:

$$\frac{\partial (\rho \vec{v})}{\partial t} + \nabla \cdot (\rho \vec{v}\vec{v}) = -\nabla p + \nabla \cdot \bar{\tau} + \rho g \qquad (2)$$

Where p is pressure (Pa)

$\bar{\tau}$ is viscous stress tensor (Pa)

g is gravitational acceleration (m/s²)

The terms on the left-hand side represent the local rate of change of momentum and the convective momentum transport due to fluid motion, respectively. The terms on the right-hand side represent the summation of external forces acting on the system, including the pressure gradient force ($-\nabla p$), the viscous shear stress tensor ($\nabla \cdot \bar{\tau}$), and the gravitational body force (ρg), which induces buoyancy effects in the domain.

Heat transfer by radiation occurs in simulation, and the Rosseland radiation model is applied, which is suitable for optically thick media.

- Energy Equation (including Rosseland radiation)

The thermal behavior and heat transfer within the system are governed by the principle of conservation of energy. In this study, the Rosseland radiation model is integrated into the energy equation, as it is highly suitable for optically thick mediums. The energy equation is expressed as:

$$\frac{\partial(\rho h)}{\partial t}+\nabla\cdot(\rho\vec{v}h)=\nabla\cdot\left[\left(k+\frac{16\sigma T^3}{3\beta}\right)\nabla T\right] \quad (3)$$

Where h is specific enthalpy (J/kg)

k is thermal conductivity (W/m·K)

σ is Stefan-Boltzmann constant 5.67×10^{-8} W/m^{2}K^4

β is Rosseland mean absorption coefficient (1/m)

T is temperature (K)

- Turbulence Model (k-ε)

To capture the turbulent behavior of the airflow, the standard k-ε turbulence model was employed. This model consists of two transport equations to resolve the turbulent kinetic energy (k) and the turbulent dissipation rate (ε), written as follows:

Turbulent kinetic energy

$$\frac{\partial(\rho k)}{\partial t}+\nabla\cdot(\rho\vec{v}k)=\nabla\cdot\left[\left(\mu+\frac{\mu_t}{\sigma_k}\right)\nabla k\right]+G_k-\rho\varepsilon \quad (4)$$

Turbulent dissipation rate

$$\frac{\partial(\rho \varepsilon)}{\partial t}+\nabla\cdot(\rho\vec{v}\varepsilon)=\nabla\cdot\left[\left(\mu+\frac{\mu_t}{\sigma_\varepsilon}\right)\nabla k\right]+C_{1\varepsilon}G_k\frac{\varepsilon}{k}-C_{2\varepsilon}\rho\frac{\varepsilon^2}{k} \quad (5)$$

Where $C_{1\varepsilon}$, $C_{2\varepsilon}$ are empirical model constants (-)

G_k is generation of turbulent kinetic energy (kg·m^1/s^3)

μ is dynamic viscosity (Pa·s)

μ_t is turbulent viscosity (Pa·s)

σ_ε is turbulent Prandtl number for ε (-)

σ_k is turbulent Prandtl number for k (-)

Simulation

This research focuses on enhancing the thermal efficiency of the solar collector without load. Therefore, simulations will be conducted to compare the performance of a solar collector in each case. For the simulation of the solar collector, a total of 16 different inlet-outlet air channel patterns will be varied (Figure 2). In addition, the air mass flow rate varies at constant values of 0.0245-0.1225 kg/s, respectively.

Thermal efficiency equation

The efficiency of the solar collector is evaluated based on thermal efficiency. This is defined as the ratio of the useful heat transferred to the fluid inside the solar collector to the total global radiation incident on the surfaces of the solar collector. The thermal efficiency of parabolic solar collectors without and integrated with paraffin-filled tubes can be expressed by the following equation:

$$\eta = \frac{\dot{m}c_{p,air}\left(T_{air,outlet} - T_{air,inlet}\right)}{A_c I} \times 100\% \qquad (6)$$

Where η is thermal efficiency (%)

$\dot{m}$ is mass flow rate (kg/s)

$C_{p,air}$ is specific heat capacity of air (J/kg·K)

$T_{air,\ inlet}$ is air inlet temperature (°C)

$T_{air,\ outlet}$ is air inlet temperature (°C)

A_c is collector surface area (m²)

I is global solar radiation (W/m²)

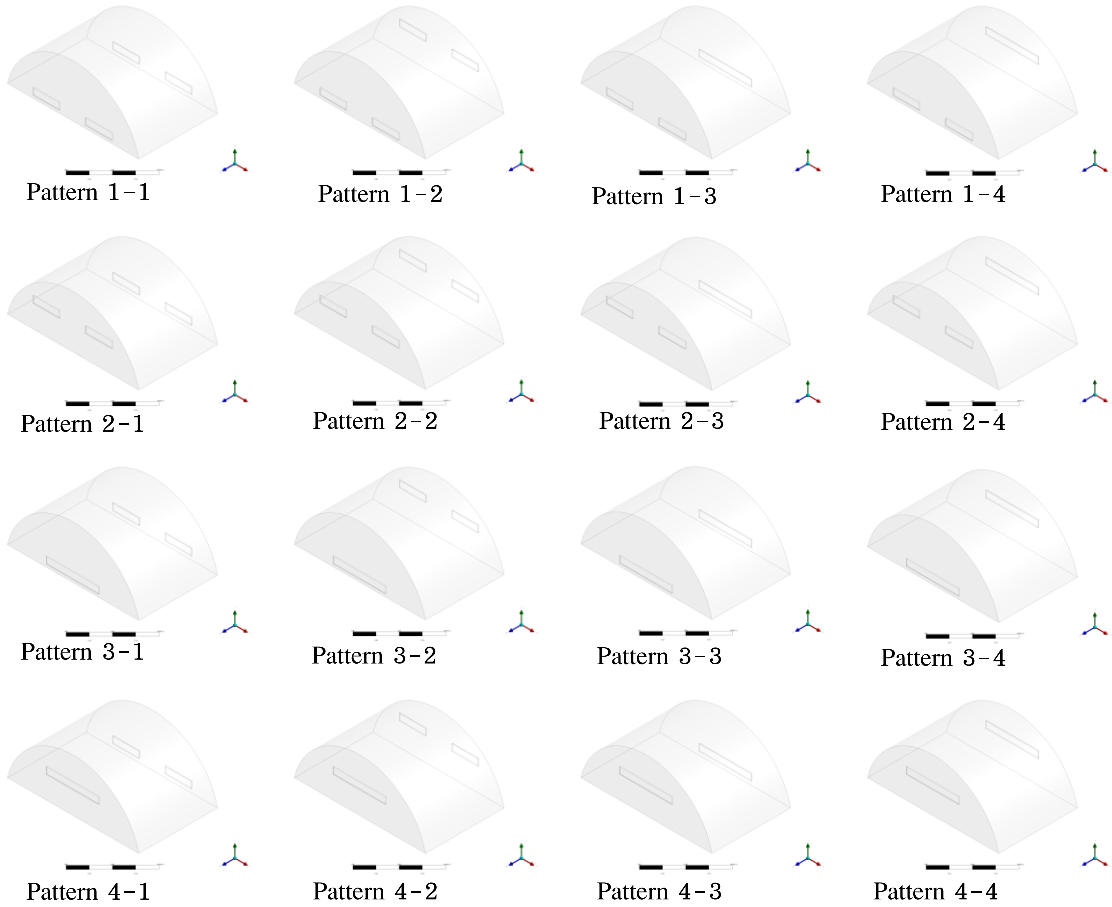

Figure 2 16 Patterns of inlet and outlet air

Experimental Setup

The experimental work was conducted at the Department of Physics, Faculty of Science, Silpakorn University, located in Nakhon Pathom, Thailand (13.82°N, 100.1°E). To capture the full range of daily thermal behavior, all experiments were conducted under varying sky conditions from 08:00 to 18:00 hours. Comprehensive data collection was implemented to allow for a detailed analysis of the thermal efficiency of the parabolic dome solar collector (PDSC).

Air outlet temperature was measured at key points throughout the collector using calibrated K-type thermocouples with an accuracy of ±0.5°C. Global solar radiation intensity was measured using a pyranometer (Kipp&Zonen, model CMP11) with an expanded uncertainty of 2.4%. The pyranometer was correctly installed at the same level as the earth's surface. All data were automatically recorded at 1-minute intervals using a multi-channel data logger (Yokogawa, model DC100). All measuring instruments were identically set up in each solar collector to prevent positioning errors (Figure 3).

PDSC performance was evaluated over at least six testing days. For accurate comparison, only days with similar total solar radiation were compared, while days with heavy rain or thick clouds were excluded. However, days with partial cloud cover were retained to reflect realistic operating conditions. After checking the raw data for errors (such as sensor signal loss), hourly and daily averages of outlet air temperature and solar radiation were calculated. These values were used to determine thermal efficiency over time and to validate the CFD simulation model in the following section.

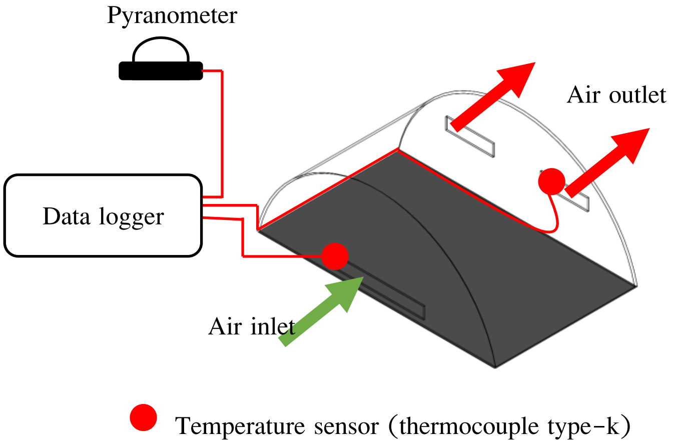

Figure 3 Experimental setup and instrument positions for the parabolic dome solar collector

Model validation

The simulation results that best matched the experimental results were identified using the coefficient of determination (R^2), which indicates the goodness of fit of the model, while mean relative deviation (MRD) and root mean square error ($RMSE$) evaluate the deviation between the experimental and simulation results (Figure.4).

$$R^2 = \frac{\sum_{i=1}^{n} (y_{simulated,i} - \bar{y})^2}{\sum_{i=1}^{n} (y_{experimental,i} - \bar{y})^2} \quad (7)$$

$$MRD = \frac{1}{n} \sum_{i=1}^{n} \left| \frac{y_{simulated,i} - y_{experimental,i}}{y_{experimental,i}} \right| \quad (8)$$

$$RMSE = \sqrt{\frac{\sum_{i=1}^{n} \left(y_{simulated,i} - y_{experimental,i} \right)^2}{n}} \quad (9)$$

Where $y_{simulated,i}$ is the simulation result of y for experiment at i , $y_{experimental,i}$ is the y value for experiment at i and $\bar{y}$ is the mean of y value.

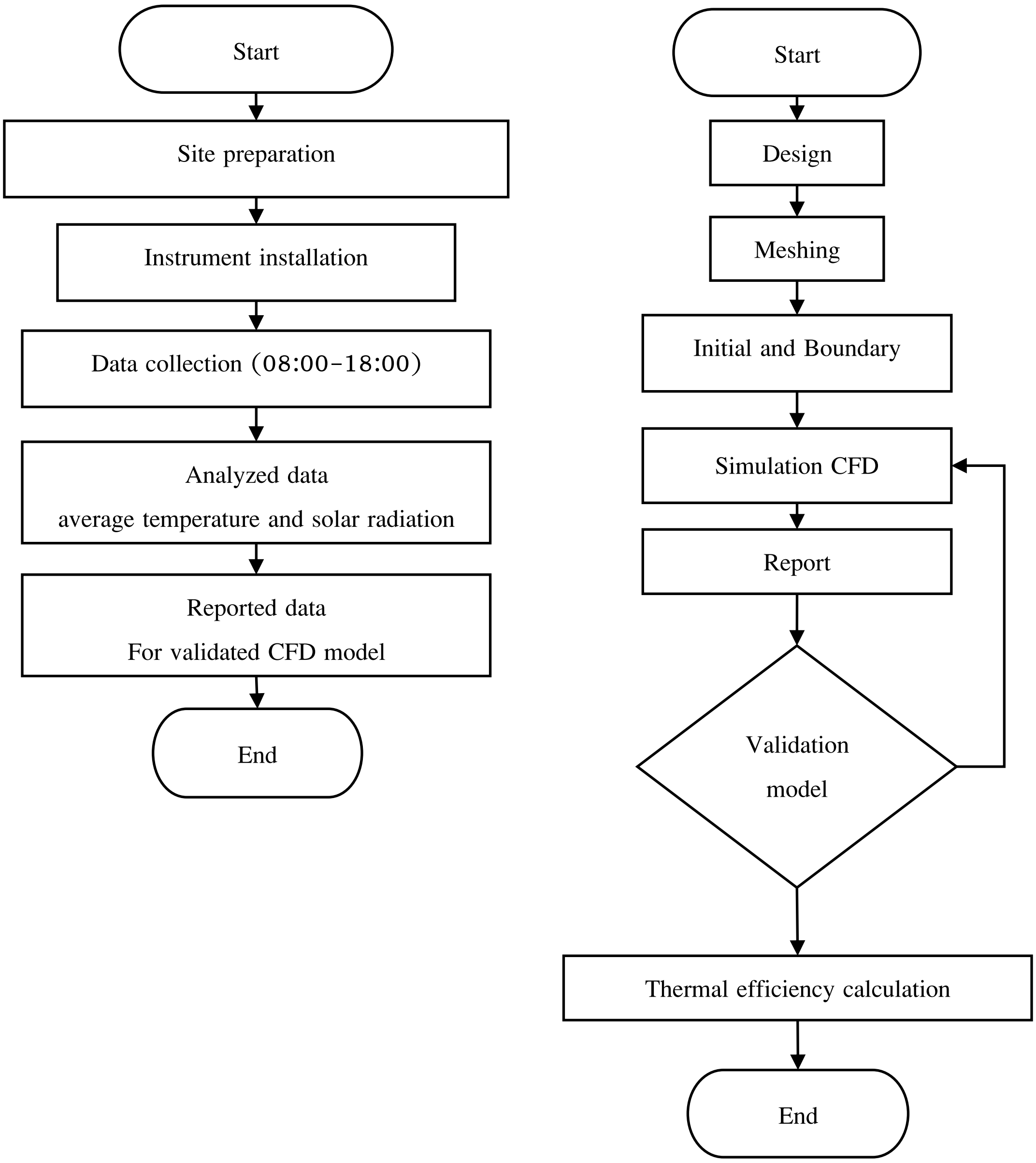

Figure 4 Flowchart of (a) experiment and (b) simulation processes

Results

Validation model

To verify the numerical framework, the simulation results were validated against experimental data. Due to manufacturing constraints for all 16 physical prototypes, validation focused solely on Pattern 3-2, the optimal pattern identified during initial screening. The simulated hourly outlet air temperatures from 6:00 h to 18:00 h closely matched the experimental trends, fluctuating with solar radiation (Fig.5). The slight discrepancies stem from environmental variations; while the actual weather fluctuated during the experiment, the ANSYS Fluent simulation used ideal conditions, resulting in slightly higher simulated air temperatures. Nevertheless, statistical validation using R^2 = 0.9942, MRD = -0.031, and RMSE = 3.656℃ confirms that the model is accurate enough to evaluate all 16 inlet-outlet patterns. These findings align with previous studies by Lokeswaran and Eswaramoorthy (2013) and Mahapatra and Tripathy (2019).

Although the statistical indicators show good overall predictive capacity, a noticeable deviation occurs between simulated and experimental temperatures during peak hours (the high-temperature region). This discrepancy is primarily due to two factors. First, environmental boundary conditions, such as ambient wind speed and solar radiation, fluctuate rapidly under natural weather, whereas the CFD setup assumes idealized, steady-state parameters for each hourly interval. Second, at high solar collector temperatures, heat losses via long-wave radiation and turbulent free convection to the ambient air become much more pronounced. The simplified radiation and thermal loss coefficients in the numerical solver may underpredict these environmental losses, leading to slightly overpredicted outlet air temperatures during peak hours. This limitation is acknowledged, and refining the thermal boundary conditions will be considered for future work.

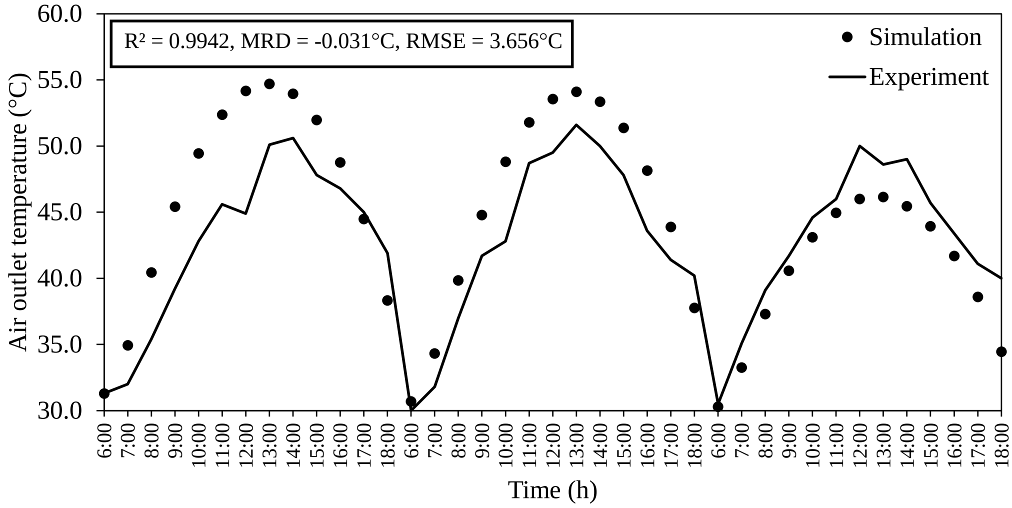

Figure 5 Comparison between simulated and experimental air outlet temperatures

Effects of inlet-outlet airflow patterns

Computational fluid dynamics (CFD) simulations across 16 air inlet and outlet patterns revealed that the inlet-outlet pattern significantly affects the air temperature distribution and airflow characteristics within the parabolic dome solar collector (PDSC). To provide clear physical insights and avoid visual overcrowding, the flow and thermal characteristics of the optimal pattern (Pattern 3-2) and the least efficient pattern (Pattern 4-1) are selectively contrasted in Figure 6 and Figure 7. The results for the remaining patterns are presented in the additional figures of the Supplement (see Figures S1-S14).

The Figure 6 illustrates the airflow velocity vectors and streamlines inside the PDSC for these two contrasting cases. In the inefficient arrangement (Pattern 4-1), air severely recirculates within localized regions. This flow recirculation creates stagnant "dead zones" where heated air becomes trapped, drastically limiting uniform heat dissipation from the absorber plates and elevating thermal losses to the polycarbonate enclosure. Conversely, Pattern 3-2 features a staggered inlet and outlet layout that forces the fluid flow to sweep across the maximum possible cross-sectional area of the absorber plate. This optimal pattern minimizes fluid bypass and stagnation, promoting a highly uniform air velocity distribution.

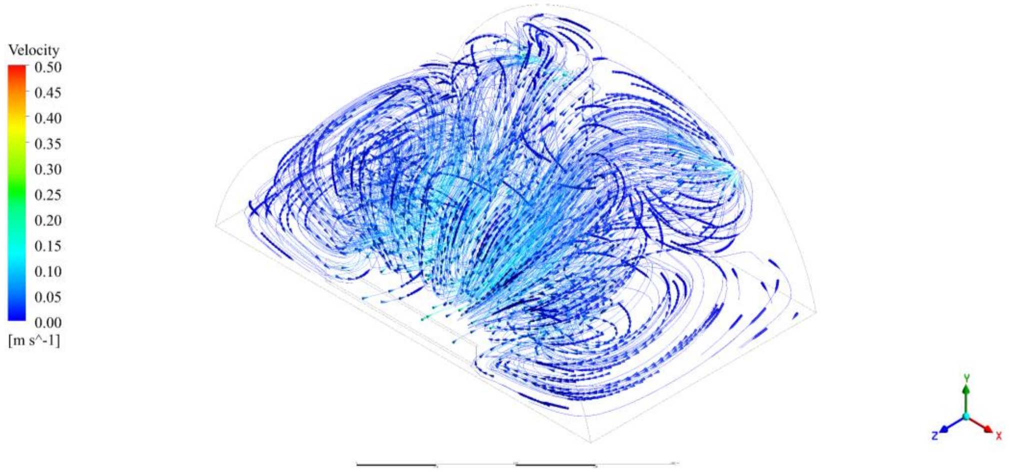

Figure 6 air distribution inside the solar collector: Pattern 3-2

To analyze the thermal impacts of these air distributions, Figure 7 presents the heating performance profiles. In the inefficient patterns, trapped air within the recirculation zones causes localized overheating without effective energy transport. However, the staggered positions in Pattern 3-2 force the airflow to cover the largest possible area of the absorber plate. This maximizes the effective heat transfer surface area and increases fluid residence time over the absorber, thereby enhancing the overall convective heat transfer rate. Consequently, instead of creating localized bypassing or low-velocity dead zones, Pattern 3-2 promotes continuous thermal interaction, allowing heat from the absorber to be efficiently carried away by the moving air mass.

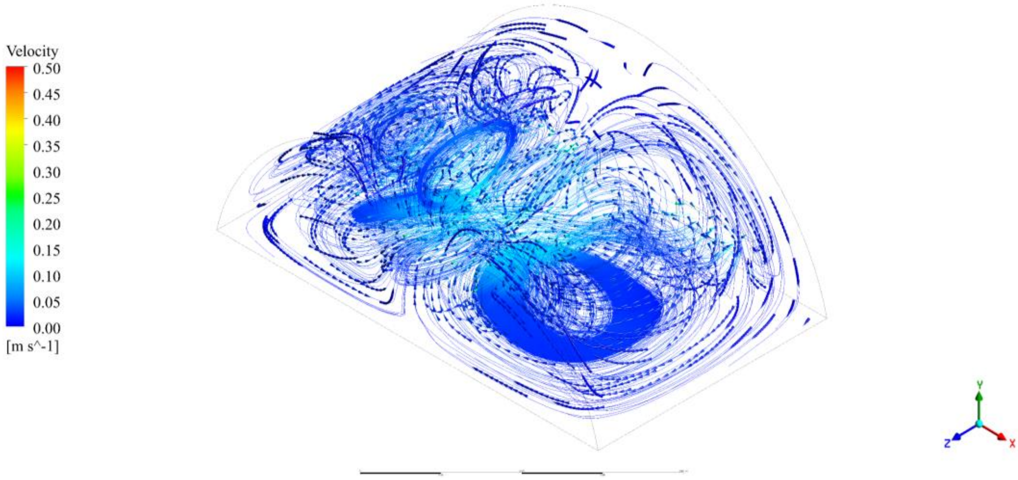

Figure 7 air distribution inside the solar collector: Pattern 4-1

The Fig. 8 presents the air outlet temperatures recorded across all 16 patterns. The results demonstrate that Pattern 3-2 consistently yields the highest outlet air temperature, while Pattern 4-1 produces the lowest. This disparity directly reflects the airflow behaviors discussed above: patterns that promote a uniform, sweeping flow allow the airstream to accumulate more thermal energy before exiting the collector, whereas patterns with stagnant dead zones trap heat locally and reduce thermal energy transfer. Consequently, the outlet temperature serves as a direct indicator of how efficiently each pattern exploits the available absorber area for convective heat exchange.

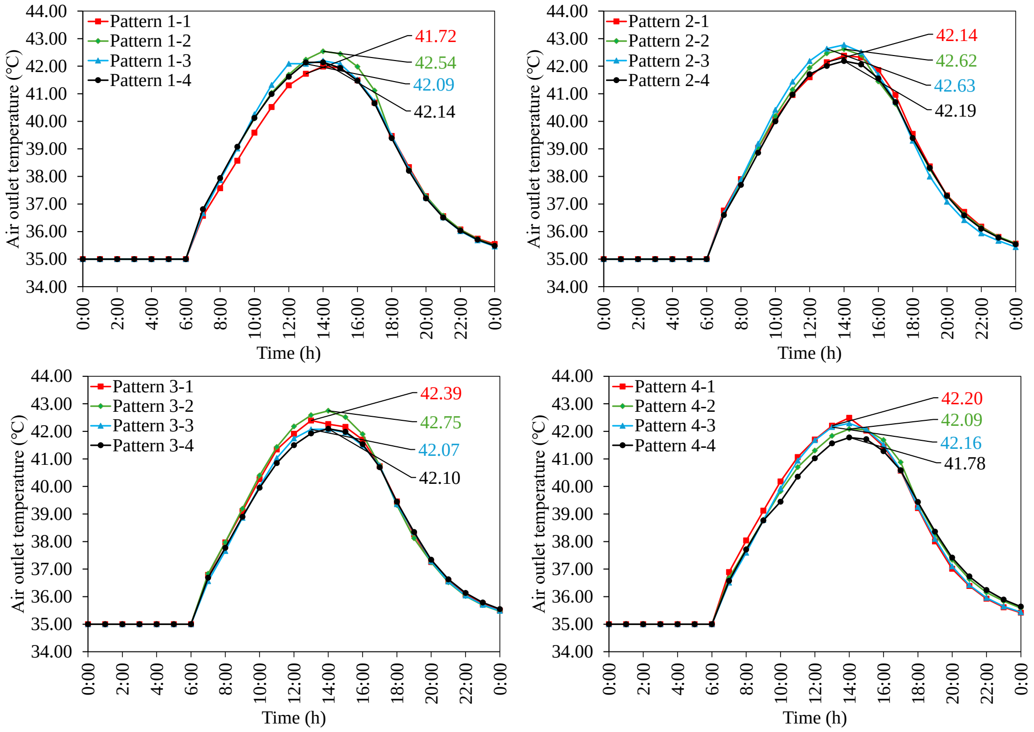

Figure 8 The air outlet temperature of the solar collector: Pattern of air inlet and outlet

As illustrated by the temperature data in Fig. 9, Pattern 3-2 yields the highest average thermal efficiency at 41.97%. This relationship confirms that the laminar and uniform flow characteristics in Figure 6 directly contribute to improved system performance. This result is consistent with the research by Rahmat et al. (2025), which indicates that airflow direction management affects heat loss: when air circulation is good, the temperature difference between the radiation plate and the air decreases, resulting in reduced heat loss to the environment.

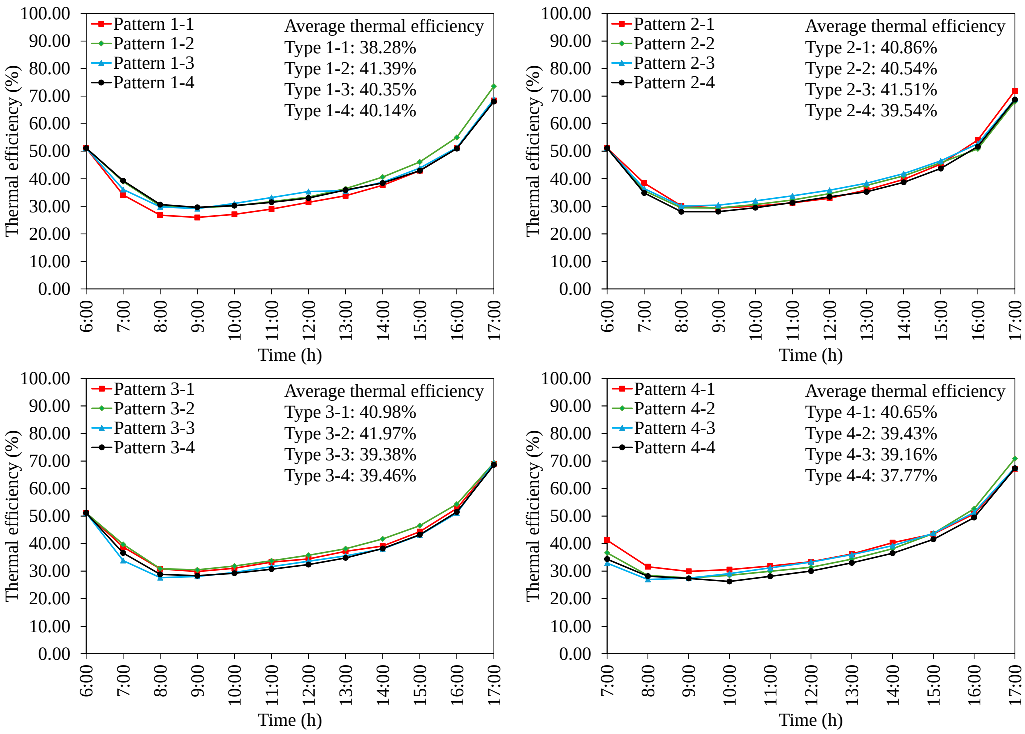

Figure 9 Thermal efficiency of the solar collector: Pattern of air inlet and outlet

Therefore, selecting a 3-2 inlet-outlet pattern not only increases the outlet air temperature but also enhances the heating stability of the parabolic solar collector. This simulation data provides a crucial guideline for the engineering design of future solar drying systems, aiming for maximum solar energy utilization under no-load conditions.

Discussion

The consistency between numerical simulation results and experimental validation results indicates that the generated CFD model accurately captures the system's thermal behavior, particularly its response to changes in solar radiation intensity over time. The close correlation between simulation and experimental results confirms the reliability of the results across 16 different inlet-outlet patterns and demonstrates the suitability of the simulation's physics settings for real-world applications.

Regarding the internal fluid dynamics, Pattern 3-2 achieved the highest average thermal efficiency at 41.97%. As visualized in the comparative flow fields of Figure [5], the staggered layout effectively minimizes the formation of stagnant 'dead zones,' which are the primary cause of localized hot spots around the solar absorbers in less efficient designs like Pattern 4. By promoting a highly uniform airflow across the entire cross-sectional area of the collector, the thermal energy is continuously and effectively transported out of the system. This collectively enhances the overall convective heat transfer rate compared to patterns plagued by severe localized internal recirculation.

This finding aligns with the study by Rahmat et al. (2025), which emphasized that optimizing the flow path and aerodynamic direction has a more direct impact on thermal efficiency than simply increasing the physical dimensions of the device. The capacity of Pattern 3-2 to deliver an average outlet air temperature of up to 42.75°C demonstrates that an optimized flow channel pattern suppresses ambient thermal losses more effectively than conventional straight-line or poorly arranged designs; the latter often suffer from severe air recirculation, trapping hot air inside the enclosure for too long and causing unwanted heat dissipation backward through the glass cover.

In summary, the discussion underscores that the physical placement of air inlets and outlets is a critical governing factor for solar collector performance. Although this investigation was conducted under a no-load scenario, the results provide a robust foundation for practical engineering design. Implementing the 3-2 pattern allows the system to maximize solar thermal utilization, serving as a critical guideline for developing high-efficiency, energy-saving solar drying systems in the future.

Limitations

Despite the promising results, several limitations of this study should be acknowledged. First, all simulations and experiments were conducted under no-load conditions, meaning no drying material was placed inside the collector. The presence of agricultural products during actual drying operations would alter the internal airflow patterns and thermal behavior, potentially affecting the relative performance ranking of the 16 inlet-outlet patterns. Second, this study evaluated a fixed set of 16 inlet-outlet patterns, and other geometric patterns may exist that could yield superior performance. Third, the PDSC dimensions used in this study were scaled down to half the length of a full-sized parabolic dome solar dryer to conserve materials and computational resources; therefore, the results may not be directly transferable to full-scale systems without further validation. Finally, the experimental data were collected specifically in Nakhon Pathom, Thailand, and the findings may vary under different climatic conditions, solar radiation intensities, or geographic locations.

Future Research

Future work will focus on integrating the optimized PDSC with the Pattern 3-2 inlet-outlet pattern into a full-scale parabolic dome solar dryer system. Experimental drying trials will be conducted to evaluate the combined system's performance under actual load conditions. The integrated system will be compared against two benchmarks: a conventional solar dryer without the PDSC, and traditional open-air sun drying. These comparisons will provide a comprehensive assessment of the energy savings, drying efficiency, and product quality improvements achievable through the optimized inlet-outlet design developed in this study.

Conclusion and Suggestions

This research investigated the design and optimization of air inlet and outlet patterns for a parabolic dome solar collector (PDSC) to enhance its preheating efficiency before integration into drying systems. The fluid flow and thermal behavior were analyzed using ANSYS Fluent, and the numerical model demonstrated high predictive accuracy and a statistically significant correlation with real-world experimental data. Based on key statistical indicators (R^2, MRD, and RMSE), the simulation framework successfully evaluated 16 different airflow patterns. The results revealed that Pattern 3-2 exhibited the most outstanding performance, achieving a maximum average thermal efficiency of 41.97% and an average outlet air temperature of 42.75°C. This superior performance is primarily attributed to the staggered air duct arrangement, which promotes a highly uniform air velocity distribution across the solar collector plate. Conversely, alternative patterns suffered from severe localized fluid recirculation and heat accumulation, leading to inefficient thermal transport. The substantial reduction of stagnant zones in Pattern 3-2 successfully optimizes the overall convective heat transfer mechanism within the system. This finding is consistent with international literature indicating that mass airflow path design is a pivotal factor in advancing the thermal output of solar collectors. Future work will focus on integrating this optimized PDSC with a parabolic dome solar dryer to comprehensively evaluate its combined thermal and drying efficiency under operational loads.

Acknowledgments

This research was financially supported by Faculty of Science, Silpakorn University. Sincere thanks are extended to Silpakorn University, for their support of research facilities and assistance.

Author Contributions

Phoothanet Saengcharoon: Methodology, Formal analysis, Writing – original draft

Orawan Aumporn: Project administration, Conceptualization, Writing – review & editing

Conflict of Interests

All authors declare that they have no conflicts of interest.

Funding

The authors received no financial support for the research of this article.

Declaration of Generative AI and AI-assisted Technologies

During the preparation of this manuscript, the authors used QuillBot for plagiarism and grammar checking and used Claude to create a graphical abstract. Following its use, the authors thoroughly reviewed and edited the content and accepted full responsibility for the last version of the publication.

References

Aghakhani, S., & Afrand, M. (2022). Experimental study of the effect of simultaneous application of the air- and water-cooled flow on efficiency in a Photovoltaic thermal solar collector with porous plates. *Applied Thermal Engineering*, *217*, 119161. https://doi.org/10.1016/j.applthermaleng.2022.119161

Demissie, P., Hayelom, M., Kassaye, A., Hailesilassie, A., Gebrehiwot, M., & Vanierschot, M. (2019). Design, development and CFD modeling of indirect solar food dryer. *Energy procedia*, *158*, 1128-1134. https://doi.org/10.1016/j.egypro.2019.01.278

Duffie, J. A., Beckman, W. A., & Blair, N. (2020). *Solar engineering of thermal processes, photovoltaics and wind.* John Wiley & Sons. https://doi.org/10.1002/9781119540328

Famiglietti, A., Lecuona-Neumann, A., Nogueira, J., & Rahjoo, M. (2020). Direct solar production of medium temperature hot air for industrial applications in linear concentrating solar collectors using an open Brayton cycle. Viability analysis. *Applied Thermal Engineering*, *169*, 114914. https://doi.org/10.1016/j.applthermaleng.2020.114914.

Hajiyat, H. R., Hussain, S. A., & Harun, M. Y. (2023). Inlet Size and Location Impact on Greenhouse Dryer Process Dynamics. *Chemical Engineering Transactions*, *106*, 1123-1128. https://doi.org/10.3303/CET23106188

Janjai, S., Lamlert, N., Intawee, P., Mahayothee, B., Bala, B. K., Nagle, M., & Müller, J. (2009). Experimental and simulated performance of a PV-ventilated solar greenhouse dryer for drying of peeled longan and banana. *Solar energy*, *83*(9), 1550-1565. https://doi.org/10.1016/j.solener.2009.05.003

Kherrafi, M. A., Benseddik, A., Saim, R., Bahaz, S., & Messeguem, T. (2025). Experimental and numerical study of performance enhancement in a direct solar dryer integrated with obstacles. *Applied Thermal Engineering*, *259*, 124942. https://doi.org/10.1016/j.applthermaleng.2024.124942

Lingayat, A., Das, P., & Chandramohan, V. P. (2025). A detailed review on performance enhancement of solar air collector systems. *Applied Thermal Engineering*, 127530. https://doi.org/10.1016/j.applthermaleng.2025.127530

Lokeswaran, S., & Eswaramoorthy, M. (2013). An experimental analysis of a solar greenhouse drier: computational fluid dynamics (CFD) validation. *Energy Sources, Part A: Recovery, Utilization, and Environmental Effects*, *35*(21), 2062-2071. https://doi.org/10.1080/15567036.2010.532195

Mahapatra, A., & Tripathy, P. P. (2019). Thermal performance analysis of natural convection solar dryers under no load condition: experimental investigation and numerical simulation. *International journal of green energy*, *16*(15), 1448-1464. https://doi.org/10.1080/15435075.2019.1671417

Mekhilef, S., Saidur, R., & Safari, A. (2011). A review on solar energy use in industries. *Renewable and sustainable energy reviews*, *15*(4), 1777-1790. https://doi.org/10.1016/j.rser.2010.12.018

Omeiza, L. A., Abid, M., Dhanasekaran, A., Subramanian, Y., Raj, V., Kozak, K., Mamudu, U., & Azad, A. K. (2024). Application of solar thermal collectors for energy consumption in public buildings–An updated technical review. *Journal of Engineering Research*, *12*(4), 994-1010. https://doi.org/10.1016/j.jer.2023.09.011

Østergaard, P. A., Duic, N., Noorollahi, Y., & Kalogirou, S. (2023). Advances in renewable energy for sustainable development. *Renewable energy*, *219*, 119377. https://doi.org/10.1016/j.renene.2023.119377

Rahmat, M. A. A., Ibrahim, A., Ishak, M. A. A., Syafiq, U., & Al-Aribe, K. M. (2025). Numerical investigation of thermal and airflow profiles in diverse solar dryer chamber configurations. *Case Studies in Thermal Engineering*, *73*, 106612. https://doi.org/10.1016/j.csite.2025.106612

Singh, A. K., & Kumar, R. (2025). Enhancing renewable energy systems using loop heat pipes: A case research on solar thermal applications. *Applied Thermal Engineering*, *275*, 126866. https://doi.org/10.1016/j.applthermaleng.2025.126866

Stevovic, I., Mirjanic, D., & Petrovic, N. (2021). Integration of solar energy by nature-inspired optimization in the context of circular economy. *Energy*, *235*, 121297. https://doi.org/10.1016/j.energy.2021.121297

Tuncer, A. D., Khanlari, A., Afshari, F., Sözen, A., Ciftci, E., Kusun, B., & Şahinkesen, İ. (2023). Experimental and numerical analysis of a grooved hybrid photovoltaic-thermal solar drying system. *Applied Thermal Engineering*, *218*, 119288. https://doi.org/10.1016/j.applthermaleng.2022.11928